ACS APPLIED MATERIALS & INTERFACES

www.acsami.org Research Article

Room-Temperature Ferroelectric $LiNb_6Ba_5Ti_4O_{30}$ Spinel Phase in a Nanocomposite Thin Film Form for Nonlinear Photonics

Jijie Huang,* Han Wang, Dongfang Li, Zhimin Qi, Di Zhang, Ping Lu, Hou-Tong Chen, Dmitry A. Yarotski, Pao-Tai Lin, Xinghang Zhang, and Haiyan Wang*

Cite This: ACS Appl. Mater. Interfaces 2020, 12, 23076−23083 Read Online

ABSTRACT: Tetragonal tungsten bronze (TTB) materials are one of the most promising classes of materials for ferroelectric and nonlinear optical devices, owing to their very unique noncentrosymmetric crystal structure. In this work, a new TTB phase of $LiNb_6Ba_5Ti_4O_{30}$ (LNBTO) has been discovered and studied. A small amount of a secondary phase, $LiTiO_2$ (LTO), has been incorporated as nanopillars that are vertically embedded in the LNBTO matrix. The new multifunctional nanocomposite thin film presents exotic highly anisotropic microstructure and properties, e.g., strong ferroelectricity, high optical transparency, anisotropic dielectric function, and strong optical nonlinearity evidenced by the second harmonic generation results. An optical waveguide structure based on the stacks of α-Si on SiO_2/LNBTO−LTO has been fabricated, exhibiting low optical dispersion with an optimized evanescent field staying in the LNBTO−LTO active layer. This work highlights the combination of new TTB material designs and vertically aligned nanocomposite structures for further enhanced anisotropic and nonlinear properties.

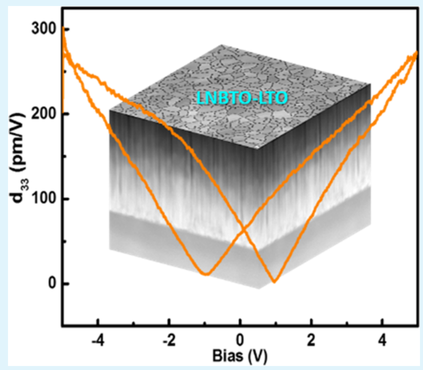

KEYWORDS: *tetragonal tungsten bronze, optical nonlinearity, ferroelectricity, vertically aligned nanocomposite, waveguide*

■ INTRODUCTION

Nonlinear optical (NLO) materials have aroused growing interests since the discovery of second-harmonic generation (SHG) in the early 1960s.[1] NLO phenomena occur when high-intensity light travels in a nonlinear medium where the polarization density responds nonlinearly to the incident electromagnetic fields. NLO materials have imposed broad impacts on information technology and photonic applications, such as waveguides, resonators, optical probes and sensors, optical data storage, optical information processing, etc.[2−7] For example, $LiNbO_3$ (LNO) is one of the most attractive NLO materials, owing to its high second-order nonlinear and electro-optical coefficients, which make it desirable for nonlinear frequency conversions and integrated optical devices,[8−10] although its optical damage threshold is relatively low. $BaTiO_3$ (BTO) is another important NLO material with strong second-harmonic generation, high third order susceptibility, as well as its successful epitaxial integration on Si.[11−13]

Searching for new NLO materials is critical toward even more pronounced nonlinearities and understanding the fundamental nonlinear polarization mechanisms. Tetragonal tungsten bronze (TTB) materials have been considered as one of the promising candidates since their NLO properties were first investigated in IBM and Bell Laboratories back in 1967.[14] TTB materials are often also accompanied by a ferroelectric response, which makes them attractive for various device applications.[15,16] In addition, the number of cationic sites in TTB materials is higher than those in traditional perovskites, which allows versatile substitutions to tailor their properties. The general chemical formula for TTB materials can be described as $(A2)_4(A1)_2(C)_4(B1)_2(B2)_8O_{30}$[17] where $B1O_6$ and $B2O_6$ are octahedra sharing corners, and A2, A1, and C are interstices (C sites are typically vacant). Some of the reported TTB materials include $Ba_5La_xSm_{1-x}Ti_3Nb_7O_{30}$,[18] $Ba_4Sm_2Fe_2Nb_8O_{30}$,[19] and so forth. However, most of the synthesized TTB materials are in bulk form;[20−22] limited efforts have been devoted to the growth of TTB thin films, especially epitaxial thin films.[23−25] Up to date, there are very limited or no prior reports on the atomic scale microstructure of the TTB thin film materials.

In this work, we demonstrate a new TTB thin film of $LiNb_6Ba_5Ti_4O_{30}$ (LNBTO) with high epitaxial quality on a $SrTiO_3$ (STO) (001) substrate using a pulsed laser deposition (PLD) technique. The crystal structure of such an LNBTO phase is revealed by detailed microstructure analysis, in both plan-view and cross-section. Furthermore, $LiTiO_2$ (LTO) is introduced as a secondary phase to form a unique vertically

Received: February 23, 2020
Accepted: April 28, 2020
Published: April 28, 2020

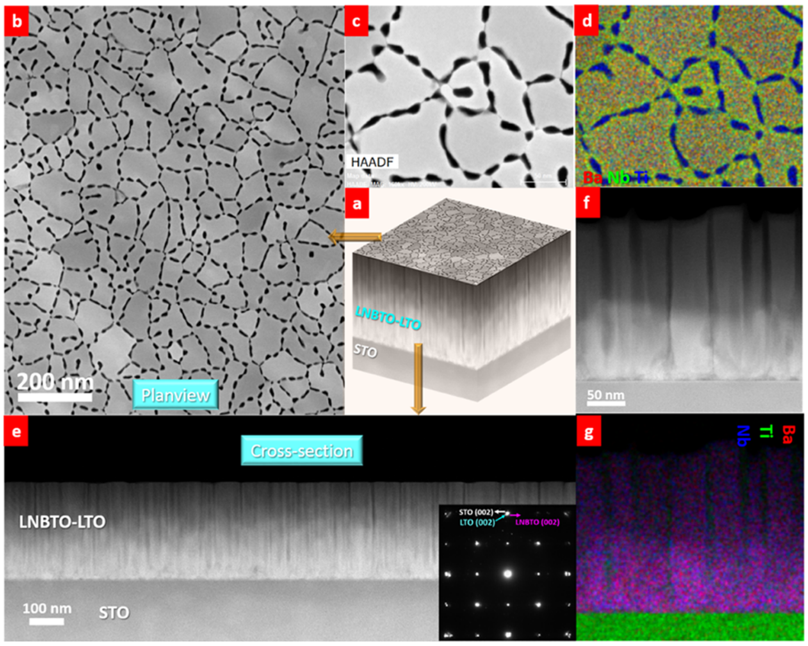

Figure 1. Overall microstructure characterization of the new nanocomposite thin film. (a) 3D overview of the sample. (b) Low-magnification plan-view STEM image and (c) typically enlarged area with (d) corresponding EDS mapping. (e) Low-magnification cross-sectional STEM image with selected area electron diffraction (SAED) patterns and (f) typical enlarged area with (g) corresponding EDS mapping.

aligned nanocomposite (VAN) structure, which provides additional tuning for the anisotropic properties, such as enhanced ferroelectric and anisotropic optical response. VAN structures have been extensively explored in oxide−oxide[26,27] and recently extended to other systems such as metal−oxide[28−30] and metal−nitride[31,32] systems. These VAN structures present highly anisotropic electrical, magnetic, and optical responses. The new TTB material in this work, combined with its unique VAN structure, paves a way toward novel NLO material designs for advanced optical devices.

■ RESULTS AND DISCUSSION

Microstructure characterization was first carried out to explore the overall crystallinity and morphology of the as-deposited film. Figure 1a is the 3D demonstration composed of low-magnification plan-view and cross-sectional STEM images. The large-scale plan-view image in Figure 1b presents a very interesting and unique nanonecklace-like structure, which can be observed more clearly in a typically enlarged area in Figure 1c (an enlarged image is shown in Figure S1 to demonstrate the uniform growth of the entire film over a large area). The corresponding EDS mapping in Figure 1d shows that Ba, Nb, and Ti exist in the main phase, and only Ti appears in the phase boundary areas (i.e., the "necklace"-like regions), which is also clearly presented in Figure S2a where line scans across a typical necklace-like area reveal the element distribution in the main phase and dark contrast phase, as shown in Figure S2b. The low-magnification cross-sectional STEM image in Figure 1e exhibits an obvious VAN structure. The enlarged area in Figure 1f and its corresponding EDS mapping in Figure 1g further confirm the element distribution in the film. Therefore, the main phase can be determined as $LiNb_xBa_5Ti_4O_y$ (Ba/Ti ratio was determined to be ∼5:4 by EDS), and the dark contrast phase at the phase boundaries is $Li_xTi_yO_z$. To further explore the two phases, standard θ−2θ XRD was conducted, and the results are plotted in Figure S3. The peak observed at 45.123° can be assigned to the $LiNb_6Ba_5Ti_4O_{30}$ (002) plane (PDF#39-0134, a tetragonal phase, $a = b = 12.4839$ Å, $c = 4.0117$ Å), and the peak at 44.3315° corresponds to the $LiTiO_2$ (002) plane (PDF#16-0223, a cubic phase, $a = b = c = 4.14$ Å). The results are consistent with the SAED pattern obtained in the cross-sectional view along the $[100]_{STO}$ in the inset of Figure 1e. Therefore, we can determine the main phase to be $LiNb_6Ba_5Ti_4O_{30}$ (LNBTO) and the dark contrast secondary phase to be $LiTiO_2$ (LTO).

To further explore and understand the epitaxial growth of the nanocomposite thin film, comprehensive microscopy study has been conducted. Figure 2a exhibits a local area to show both phases in plan view, and Figure 2b shows the LNBTO phase in an atomic scale where periodic lattice arrangement can be clearly observed. The unit cell in Figure 2c matches well with TTB crystal structure as shown in Figure 2d (the square symbol presents one unit cell), which confirms a new synthesized TTB phase. The complex in-plan SAED patterns (see Figure S4) can be decomposed into two sets of subpatterns, as illustrated by orange and blue dots in Figure 2e, resulting from the in-plane rotation (∼37°) of two equivalent domains (some weak diffraction dots could be identified and attributed to the LTO phase). This is further confirmed by the φ scan of LNBTO (420) and STO (110) (see Figure S5), revealing a 37° rotation between two LNBTO domains and perfect matching between LNBTO {420} and STO {110} planes. The results agree well with the SAED pattern in Figure 2e, and the overall orientation relationship between LNBTO and STO can be determined as LNBTO (420)//STO (110) and LNBTO $[1\bar{3}0]$//STO [010] or LNBTO [310]//STO [100]. Furthermore, the atomic resolution plan-view STEM image of the secondary LTO phase is shown in Figure 2f and exhibits high epitaxial quality with in-plane d spacing of 2.10 Å. Figure 2g presents the cross-sectional view along the $[100]_{STO}$ direction, showing the interface area between the LNBTO and LTO phases where

https://dx.doi.org/10.1021/acsami.0c03487
ACS Appl. Mater. Interfaces 2020, 12, 23076−23083

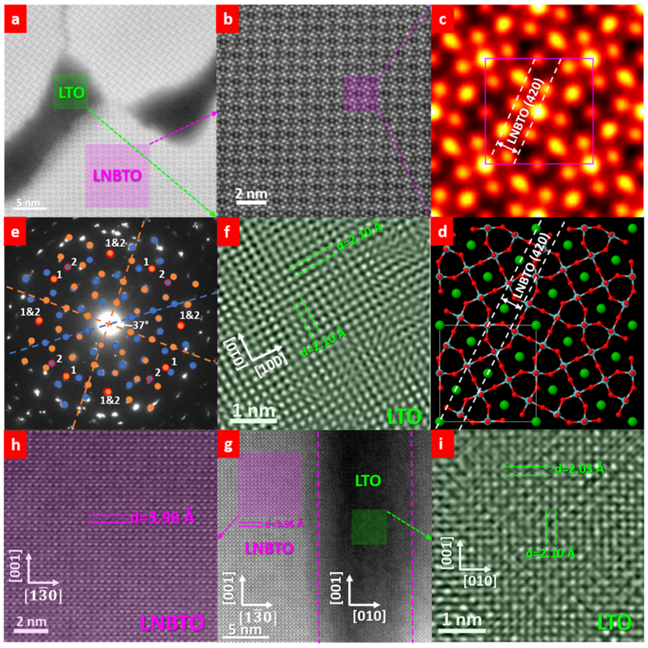

Figure 2. Detailed microstructure study on the VAN structure. (a) Plan-view STEM image to show both LNBTO and LTO phases. (b) Enlarged LNBTO area. (c) Atomic-scale STEM image to show one unit cell of the new LNBTO phase and (d) its crystal structure in-plane. (e) SAED pattern of a plan-view sample. (f) High-resolution STEM image of the dark contrasted LTO phase. (g) Cross-sectional STEM image showing the interface area. High-resolution STEM image of the (h) LNBTO and (i) LTO phases.

LNBTO and LTO are in [310] and [100] directions, respectively. Figure S6 shows the simulated (in kinetic approximation) electron diffraction pattern of LNBTO in the [310] direction. The (001) plane spacing of LNBTO can be estimated as ~3.96 Å from the high-resolution STEM image in Figure 2h, and the LNBTO (001) plane is in parallel with the STO (001) plane, consistent with the orientation relationship described earlier. Additionally, the LTO (002) plane spacing is estimated to be 2.03 Å from the atomic-scale STEM image in Figure 2i, corresponding to an out-of-plane lattice parameter about 4.06 Å, which indicates the presence of an out-of-plane compressive strain in the LTO phase due to the LNBTO phase. The composition of the LTO phase could be tuned by varying the target composition. In addition, such secondary phase could be other materials, such as $LiNbO_3$. For example, as shown in Figure S7, the TEM images demonstrate the successful growth of the nanocomposite thin film of LNBTO and $LiNbO_3$.

Ferroelectricity is one of the most intriguing properties for TTB materials, and therefore, we conducted a piezoelectric force microscopy (PFM) study to investigate the local ferroelectric response of the new LNBTO−LTO nanocomposite. A poling process was first conducted by first applying a DC bias of +10 V to a 5 μm × 5 μm square and then −10 V to reverse the polarization over a 2 μm × 2 μm square centered at the previous 5 μm × 5 μm square. The resultant out-of-plane amplitude and phase switching maps are presented in Figure 3a,b, respectively. Obvious color contrast is observed for the different writing regions, which indicates the ferroelectric nature of the film. Furthermore, a butterfly-like displacement−voltage (*D*−*V*) loop (red curve in Figure S8) and the hysteresis phase−voltage loop with a sharp 180°

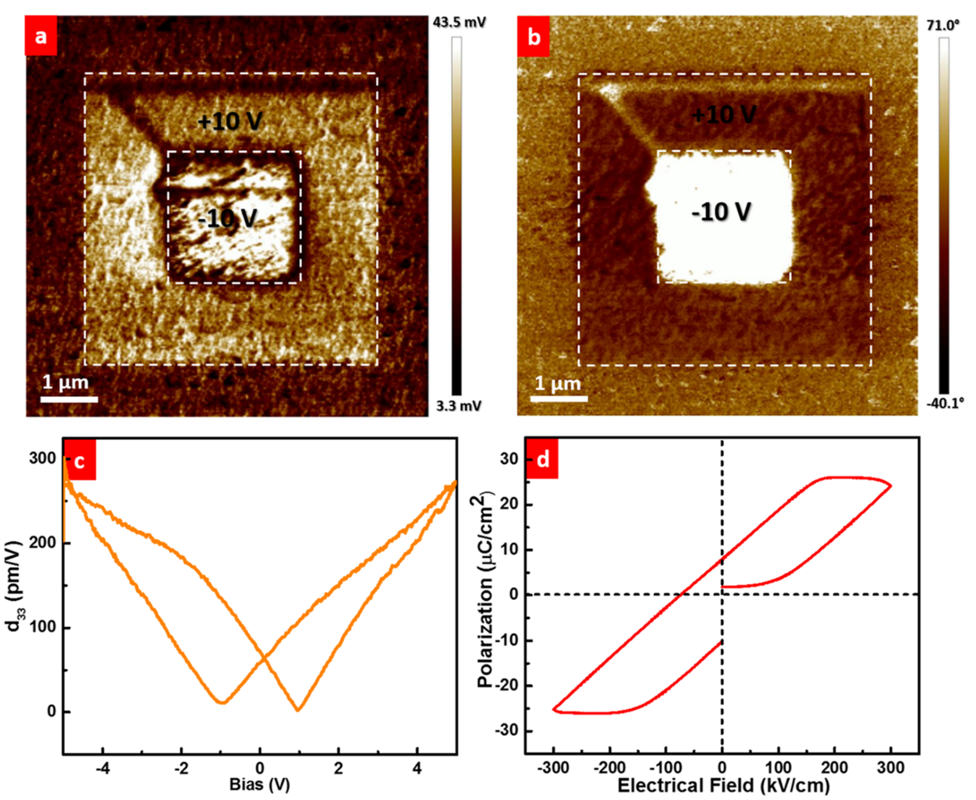

Figure 3. Ferroelectric measurements of the LNBTO−LTO nanocomposite thin film. The out-of-plane (a) amplitude and (b) phase switching maps. (c) Piezoelectric coefficient d_{33}−voltage (d_{33}−V) curve. (d) Polarization hysteresis measurement.

https://dx.doi.org/10.1021/acsami.0c03487
ACS Appl. Mater. Interfaces 2020, 12, 23076−23083

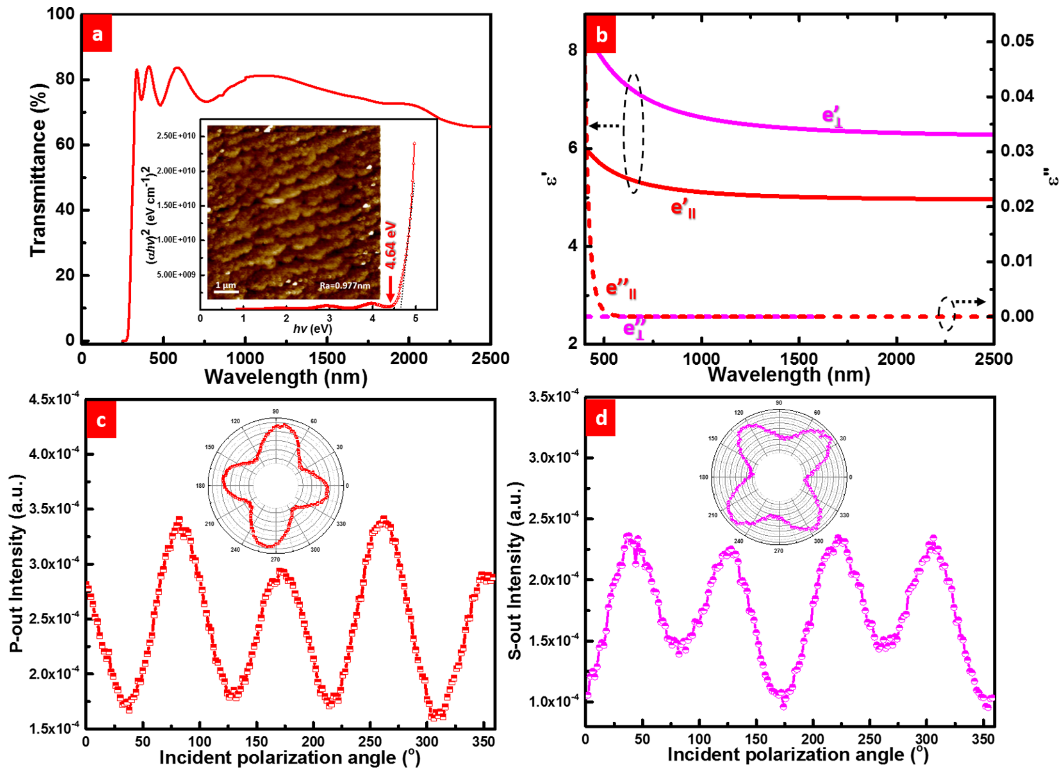

Figure 4. Optical characterizations on the new LNBTO−LTO nanocomposite thin film. (a) Transmittance measurement of the film from 250 to 2500 nm, inset is the derived Tauc plot and AFM image of a typical film surface. (b) Real and imaginary parts of the complex dielectric function of the film. SHG intensity versus incident polarization angle with output polarization fixed at (c) 0° (P-out) and (d) 90° (S-out).

change (blue curve in Figure S8) demonstrate the excellent ferroelectric switching behavior of the film. Based on the $D-V$ "butterfly" curves, the piezoelectric coefficient d_{33}−voltage ($d_{33}-V$) loop (Figure 3c) is given by $d_{33} = A_d/V_{ac}$,[33,34] where A_d is the amplitude of the electric-field-induced deformation (pm), and V_{ac} is the amplitude of the testing ac voltage (V). The $d_{33}-V$ loop clearly shows the switchable piezoelectric behavior of the nanocomposite film with an estimated maximum d_{33} value of ∼270 pm/V, which indicates that the thin film can be used as an environment-friendly lead-free piezoelectric material. To further investigate the ferroelectric behavior of the entire film, the polarization−electric field ($P-E$) loop was measured at room temperature. The well-defined hysteresis loop presented in Figure 3d shows that the saturation polarization (P_s) is 26 μC/cm^2 and exhibits the remnant polarization (P_r) of 8.1 μC/cm^2 for a coercive field (E_c) of 74.6 kV/cm, which is in the same range as or higher than those of other ferroelectric materials such as LNO or BTO.[35,36]

This new LNBTO-based nanocomposite thin film exhibits very interesting optical properties, such as high transparency, anisotropic performance, and strong nonlinearity. Optical transmission measurements have shown that the film (note that a companion sample grown on a MgO substrate has been used for the transmittance measurement since the band gap of STO is relatively low, which might block the band edge of the film) is highly transparent from ∼310 to 2500 nm, as shown in Figure 4a. Spectral oscillation was observed, indicating a smooth surface and high-quality film, which was further confirmed by the atomic force microscopy (AFM) image shown in the inset to Figure 4a with a small roughness of R_a = 0.977 nm. The optical bandgap of this nanocomposite thin film was estimated to be E_g = 4.64 eV from the Tauc plot shown in the inset of Figure 4a. Angular-dependent ellipsometry measurements were conducted to further investigate the optical properties of the film, and its complex dielectric function (real part ε' and imaginary part ε'') was derived by fitting the ellipsometric psi (φ) values (see Figure S9) by applying a uniaxial model because of the anisotropic nature of the nanocomposite film. As plotted in Figure 4b, the real part of the dielectric function exhibits different values but with similar wavelength dependence in the ordinary ($\varepsilon_{\parallel}'$) and extraordinary ($\varepsilon_{\perp}'$) directions. For the imaginary part, both $\varepsilon_{\parallel}''$ and $\varepsilon_{\perp}''$ are close to zero throughout the entire measured wavelength range, suggesting high transparency of the thin film, and are consistent with the transmittance measurements. The effective complex refractive index (refractive index n, extinction coefficient k) is presented in Figure S10. In order to investigate the NLO properties of the composite film, we also measured the SHG (excitation at 800 nm and SHG at 400 nm) as a function of polarization angle of the incident beam with output polarization fixed at 0 (P-out) and 90° (S-out), with the results shown in Figure 4c,d, respectively. The strong SHG signal could be attributed to two factors: (i) the LNBTO phase, owing to its noncentrosymmetric crystal structure; and (ii) the interface between LNBTO and LTO.

The new tetragonal tungsten bronze phase LNBTO enriches the materials library for the design of nonlinear optical devices and components. Compared to some typical ferroelectric materials, such as $BaTiO_3$(BTO), the TTB phase in this work is more reliable in terms of growth reproducibility and film uniformity, i.e., no or very little difference from area to area in the film. Therefore, as a new ferroelectric and nonlinear material, it is certainly of interests to demonstrate the

https://dx.doi.org/10.1021/acsami.0c03487
ACS Appl. Mater. Interfaces 2020, 12, 23076−23083

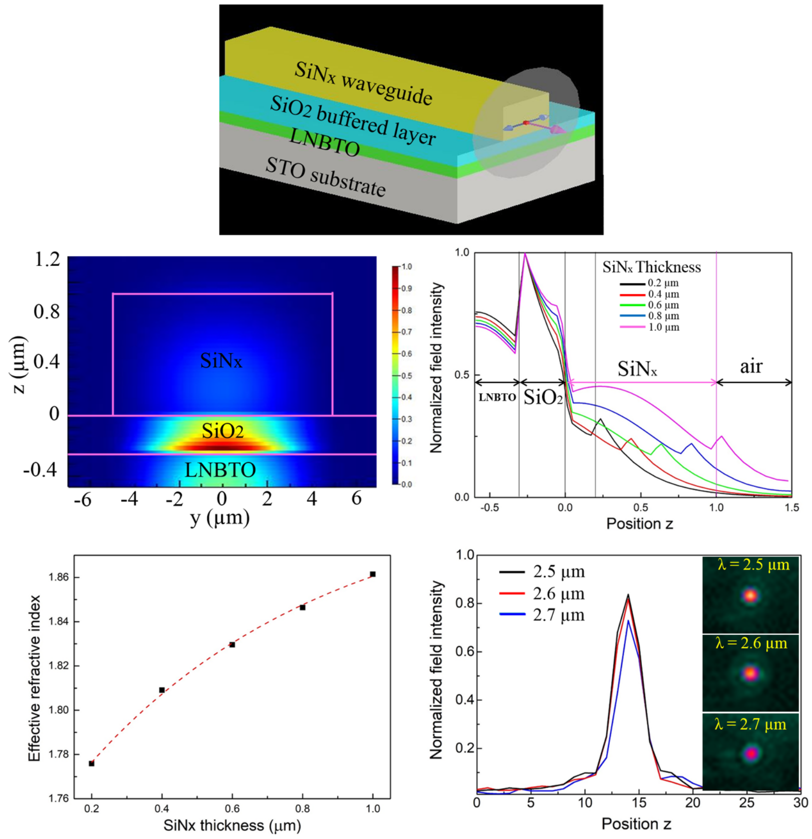

Figure 5. Demonstration of α-Si-based waveguide on a SiO_2/LNBTO−LTO multilayer stack. (a) Schematic configuration of SiN_x on the LNBTO−LTO waveguide. (b) FEM simulation of the optical waveguide mode at λ = 2.5 μm. The mode intensity was confined inside the SiO_2-buffered layer, and the evanescent field extended to the adjacent SiN_x and the LNBTO−LTO layers. (c) Calculated 1D mode profiles when the thickness of the SiN_x layer, T_{SiN}, increased from 0.2 to 1 μm. (d) Calculated effective refractive index of the waveguide when T_{SiN} increases from 0.2 to 1 μm. (e) Waveguide modes at wavelengths of 2.5, 2.6, and 2.7 μm, respectively. Similar mode profiles were similar in those three wavelengths.

feasibility of this new VAN film for waveguide application. Here, we present an integrated SiN_x/LNBTO−LTO slot waveguide structure, as schematically illustrated in Figure 5a. The SiN_x ridge (slab layer) and the buffered SiO_2 (slot layer) were created on the LNBTO−LTO (slab) functional layer. We first numerically calculated the field distribution of the propagation mode within different material layers using finite element methods (FEM) upon the excitation at λ = 2.5 μm (Figure 5b) in which the following values of refractive indices have been used: n_{SiN} = 2.10, n_{SiO2} = 1.45, $n_{LNBTO-LTO}$ = 2.27, and n_{STO} = 2.25. With a 1 μm-tall SiN_x ridge, the mode in the submicron slot is transverse magnetic (TM) polarized with the optical field mainly confined inside the SiO_2-buffered layer and field extended into the top SiN_x layer and the lower LNBTO−LTO functional layer. The latter enables light interaction with the grown ferroelectric layer, thereby realizing active optical functionalities. To further analyze the field distribution of the propagation mode, 1D field profiles with different SiN_x ridge heights are plotted in Figure 5c. When the SiN_x ridge height is reduced from 1 to 0.2 μm, the fields in both SiN_x and LNBTO−LTO decrease, and light is mostly localized in the SiO_2-buffered layer. This provides a simple route to tune the confinement of the light wave and its interaction with the LNBTO−LTO layer by changing the height of the SiN_x ridge. In addition, the effective refractive index n becomes larger for the thicker SiN_x layer (shown in Figure 5d). Therefore, we chose the 1 μm SiN_x structure in the actual device fabrication to maximize the light confinement. For the fabricated waveguide, its optical properties were evaluated using a testing station. As shown in Figure 5e, a clear fundamental mode was captured by the mid-IR camera at wavelengths ranging from λ = 2.5 to λ = 2.7 μm with similar mode profiles. At the same time, there is no mode deformation observed, which indicated a flat sidewall and smooth interfaces among SiN_x, buffered SiO_2, and LNBTO−LTO layers.

The demonstration of this unique LNBTO nanocomposite thin film with a TTB phase gives rise to a new VAN structure design. This nanocomposite thin film exhibits room-temperature ferroelectricity, which is comparable or better than some of the representative ferroelectric oxides such as BTO and LNO.[35,36] In addition, the introduction of the secondary phase provides more optical anisotropy and strong nonlinearity, owing to the high-density vertical interface region. Besides searching for a new nanocomposite system, one main effort needed is to grow a single-domain LNBTO phase. The LNBTO in this work presents two primary domains with 37° in-plane rotation, and the domain boundaries could be eliminated to further enhance the overall ferroelectric and optical properties. Potential methods include selecting appropriate substrate, such as miscut STO substrates,[37] or oblique-angle deposition (OAD) with a small angle substrate tilt.[38] Furthermore, it is expected that the other TTB-based materials can also be grown into thin film structures, such as $Ba_4Sm_2Fe_2Nb_8O_{30}$ and $Ba_5La_xSm_{1-x}Ti_3Nb_7O_{30}$, previously reported.[18,19] It is also interesting to prepare the bulk counterparts of pure $LiNb_6Ba_5Ti_4O_{30}$ to compare with the new TTB phase identified in this work. Overall, the discovery of the new tetragonal tungsten bronze phase of LNBTO provides strong electrical and optical anisotropy, nonlinearity, very high film quality, and smooth film surface, all important toward new room-temperature ferroelectric material designs and nonlinear optic component designs.

■ CONCLUSIONS

A new highly epitaxial vertically aligned nanocomposite (VAN) system based on LNBTO, a newly discovered tetragonal tungsten bronze phase, has been designed and successfully fabricated by PLD. Highly epitaxial LNBTO phase coupled with a vertically aligned LTO secondary phase present a novel VAN structure. The LNBTO phase shows two primary domains with 37° in-plane rotation to compensate the in-plane mismatch with the STO substrate. Both the strong nonlinear structure of the LNBTO phase and the LTO VAN structure result in the strong ferroelectric response and SHG signals along with many other interesting optical properties, such as high transparency in the visible and near-infrared wavelength regime, anisotropic complex dielectric function, and optical smooth surface. Finally, α-SiN_x-based waveguide on SiO_2/LNBTO−LTO has been successfully fabricated and demonstrates the power of this new nonlinear nanocomposite material and its feasibility of integration with Si-photonic devices.

■ MATERIALS AND METHODS

Target and Thin Film Preparation. The nanocomposite target was made by a standard solid-state mixing approach followed by a high-temperature sintering process. Specifically, high-purity $LiNbO_3$, Ba_2CO_3, and TiO_2 powders were first mixed and pressed into a pellet with diameter of 1 in., then it was sintered at 1300 °C for 6 h in air. The thin film was deposited on an STO (001) substrate using a PLD system with a KrF excimer laser (Lambda Physik, λ = 248 nm). The optimized deposition parameters were as follows: a deposition temperature of 700 °C, 100 mTorr of O_2 inflowing during deposition, target−substrate distance of 4.5 cm, and deposition frequency of 5 Hz. Before deposition, the base pressure was pumped down to lower than 1×10^{-6} Torr.

Microstructure Characterizations. The crystallinity of the film was characterized by XRD (Panalytical X'Pert X-ray diffractometer). An FEI Titan G2 80−200 STEM with a Cs probe corrector and ChemiSTEM technology (X-FEG and SuperX EDS with four windowless silicon drift detectors) operated at 200 kV was applied for the microstructure study. STEM using a high-angle annular dark-field (HAADF) detector and energy-dispersive x-ray spectroscopy (EDS) were employed for high-resolution imaging and EDS mapping.

Ferroelectric Measurements. Ferroelectric polarization−electric field (P−E loops) measurement was carried out by a Precision LC II Ferroelectric tester (Radiant Technologies, Inc.). The phase and amplitude maps and hysteresis loops were collected using a conductive Pt−Ir coated Si tip (model: SCM-PIT V2) with a Bruker Dimension Icon AFM.

Optical Measurements. Transmittance measurement was carried out using UV−visible spectroscopy (Lambda 1050). Variable angle ellipsometry experiments were conducted by an RC2 spectroscopic ellipsometer (J.A. Woollam Company). Two parameters of psi (ψ) and delta (Δ) correlated to the ratio of the reflection coefficients for the light of p polarization r_p and s polarization r_s: $r_p/r_s = \tan(\psi)\exp(i\Delta)$, were collected by the measurements. Afterward, the effective refractive index and optical dielectric functions were extracted by fitting the ellipsometry data using appropriate models in the VASE software. Here, a biaxial layer with general oscillator layer models consisting of hybrid Tauc−Lorentz oscillators and Drude oscillators have been applied to fit $\varepsilon_\perp$ and $\varepsilon_\parallel$, respectively.

Waveguide Fabrication. A 300 nm-thick SiO_2 and 1 μm SiN_x were deposited on a 300 nm-thick LNBTO−LTO thin film by PECVD at 350 °C, successively. Next, a negative tone photoresist was patterned on the top SiN_x layer to define the etching area. The developed photoresist had a negative-sloping sidewall to better process the lift-off step afterward. A layer of 50 nm Cr was then deposited by electron beam evaporation, which is the etching mask to define the waveguide structure. During the plasma etching process, CHF_3 and O_2 were utilized to remove the SiN_x. At last, an array of 1 μm-high SiN ridge waveguides was obtained on the SiO_2-buffered and LNBTO−LTO layers.

Waveguide Simulation. Numerical calculations were conducted to simulate the waveguide modes at λ = 2.5 μm. The simulations were taken by a two-dimensional finite element method (FEM). The size of the SiN_x waveguide is 10 μm wide and 1 μm high. Underneath the waveguide, there is a 0.3 μm-thick SiO_2-buffered layer and another 300 nm-thick LNBTO−LTO active layer. The whole device was fabricated on the STO substrate. The refractive indices are n_{SiN} = 2.10, n_{SiO2} = 1.45, calculated $n_{LNBTO-LTO}$ = 2.27, and n_{STO} = 2.25 respectively. A 10 μm × 10 μm light source was applied to excite the waveguide mode because its size is close to the mid-IR fiber, which has a core diameter of 9 μm.

Waveguide Characterization. To characterize the performance of the fabricated waveguide, a broad mid-IR test station was built. The light source is a pulsed laser with a tunable wavelength and an emission linewidth of 3 cm^{-1}. Its pulse repetition rate is 150 kHz, its pulse duration is 10 ns, and its average power is 150 mW. The probe light is first collimated into a fluoride fiber (9 μm core and 125 μm cladding) by a reflective lens and then butt coupled into the waveguide. The core of the mid-IR fiber is lined up with the smoothly cleaved front facet of the waveguide. A calcium fluoride biconvex lens (25 mm focal length) was used to focus the mid-IR signals from the waveguides, and then a liquid nitrogen cooled 640 × 512 pixel InSb camera was employed for imaging.

■ ASSOCIATED CONTENT

Supporting Information

The Supporting Information is available free of charge at https://pubs.acs.org/doi/10.1021/acsami.0c03487.

> Large-scale plan-view STEM image, EDS mapping and line scan, θ−2θ XRD scan, raw SEAD pattern, φ scans, simulated electron diffraction pattern, microstructure characterization, phase and amplitude switching behavior, ellipsometric parameter (φ) versus wavelength of the film, and refractive index and extinction coefficient of the complex refractive index of the film (PDF)

■ AUTHOR INFORMATION

Corresponding Authors

Jijie Huang − *School of Materials, Sun Yat-Sen University, Guangzhou, Guangdong 510275, China; School of Materials Engineering, Purdue University, West Lafayette, Indiana 47906, United State*; Email: huangjj83@mail.sysu.edu.cn

Haiyan Wang − *School of Materials Engineering and School of Electrical and Computer Engineering, Purdue University, West Lafayette, Indiana 47906, United State*; orcid.org/0000-0002-7397-1209; Email: hwang00@purdue.edu

Authors

Han Wang − *School of Materials Engineering, Purdue University, West Lafayette, Indiana 47906, United State*

Dongfang Li − *Center for Integrated Nanotechnologies, Los Alamos National Laboratory, Los Alamos, New Mexico 87545, United States*

Zhimin Qi − *School of Materials Engineering, Purdue University, West Lafayette, Indiana 47906, United State*

Di Zhang — *School of Materials Engineering, Purdue University, West Lafayette, Indiana 47906, United State*
Ping Lu — *Sandia National Laboratories, Albuquerque, New Mexico 87185, United States*
Hou-Tong Chen — *Center for Integrated Nanotechnologies, Los Alamos National Laboratory, Los Alamos, New Mexico 87545, United States;* orcid.org/0000-0003-2014-7571
Dmitry A. Yarotski — *Center for Integrated Nanotechnologies, Los Alamos National Laboratory, Los Alamos, New Mexico 87545, United States*
Pao-Tai Lin — *Department of Electrical and Computer Engineering, Texas A&M University, College Station, Texas 77843, United States;* orcid.org/0000-0002-5417-6920
Xinghang Zhang — *School of Materials Engineering, Purdue University, West Lafayette, Indiana 47906, United State*

Complete contact information is available at:
https://pubs.acs.org/10.1021/acsami.0c03487

Notes

The authors declare no competing financial interest.

■ ACKNOWLEDGMENTS

J.H. and H.W. acknowledge the support from the Basil S. Turner Chair Professorship at Purdue University for the seminal work. Z. Q. and H.W. acknowledge the support from the U.S. National Science Foundation (Ceramic Program, DMR-1565822 for high-resolution STEM and DMR-1809520 for thin film growth). This work was performed, in part, at the Center for Integrated Nanotechnologies, an Office of Science User Facility operated for the U.S. Department of Energy (DOE) Office of Science. Los Alamos National Laboratory, an affirmative action equal opportunity employer, is managed by Triad National Security, LLC for the U.S. Department of Energy's NNSA under contract 89233218CNA000001. Sandia National Laboratories is a multiprogram laboratory managed and operated by National Technology and Engineering Solutions of Sandia, LLC, a wholly owned subsidiary of Honeywell International, Inc., for the U.S. Department of Energy's National Nuclear Security Administration under contract DE-NA0003525. This paper describes objective technical results and analysis. Any subjective views or opinions that might be expressed in the paper do not necessarily represent the views of the U.S. Department of Energy or the United States Government.

■ REFERENCES

(1) Franken, P. A.; Hill, A. E.; Peters, C. W.; Weinreich, G. Generation of Optical Harmonics. *Phys. Rev. Lett.* **1961**, *7*, 118.
(2) Lu, H.; Liu, X.; Wang, L.; Gong, Y.; Mao, D. Ultrafast All-Optical Switching in Nanoplasmonic Waveguide with Kerr Nonlinear Resonator. *Opt. Express* **2011**, *19*, 2910−2915.
(3) Nakayama, Y.; Pauzauskie, P. J.; Radenovic, A.; Onorato, R. M.; Saykally, R. J.; Liphardt, J.; Yang, P. Tunable Nanowire Nonlinear Optical Probe. *Nature* **2007**, *447*, 1098−1101.
(4) Liu, Q.; Fukaya, T.; Tominaga, J.; Kuwahara, M.; Shima, T.; Kim, J. Nonlinear Features and Response Mechanisms of A PtO_2 Mask Layer for Optical Data Storage with A Superresolution Near-Field Structure. *Opt. Lett.* **2003**, *28*, 1805−1807.
(5) Prior, J.; Castro, E.; Chin, A. W.; Almeida, J.; Huelga, S. F.; Plenio, M. B. Wavelet Analysis of Molecular Dynamics: Efficient Extraction of Time-Frequency Information in Ultrafast Optical Processes. *J. Chem. Phys.* **2013**, *139*, 224103.
(6) Christodoulides, D. N.; Lederer, F.; Silberberg, Y. Discretizing Light Behaviour in Linear and Nonlinear Waveguide Lattices. *Nature* **2003**, *424*, 817−823.
(7) Huang, J.; Jin, T.; Misra, S.; Wang, H.; Qi, Z.; Dai, Y.; Sun, X.; Li, L.; Okkema, J.; Chen, H.-T.; Lin, P.-T.; Zhang, X.; Wang, H. Tailorable Optical Response of Au-$LiNbO_3$ Hybrid Metamaterial Thin Films for Optical Waveguide Applications. *Adv. Opt. Mater.* **2018**, *6*, 1800510.
(8) Nie, W. Optical Nonlinearity: Phenomena, Applications, and Materials. *Adv. Mater.* **1993**, *5*, 520−545.
(9) Tu, D.; Xu, C. N.; Yoshida, A.; Fujihala, M.; Hirotsu, J.; Zheng, X. G. $LiNbO_3$:Pr^{3+}: A Multipiezo Material with Simultaneous Piezoelectricity and Sensitive Piezoluminescence. *Adv. Mater.* **2017**, *29*, 1606914.
(10) Ievlev, A. V.; Alikin, D. O.; Morozovska, A. N.; Varenyk, O. V.; Eliseev, E. A.; Kholkin, A. L.; Shur, V. Y.; Kalinin, S. V. Symmetry Breaking and Electrical Frustration during Tip-Induced Polarization Switching in the Nonpolar Cut of Lithium Niobate Single Crystals. *ACS Nano* **2015**, *9*, 769−777.
(11) Eltes, F.; Caimi, D.; Fallegger, F.; Sousa, M.; O'Connor, E.; Rossell, M. D.; Offrein, B.; Fompeyrine, J.; Abel, S. Low-Loss $BaTiO_3$-Si Waveguides for Nonlinear Integrated Photonics. *ACS Photonics* **2016**, *3*, 1698−1703.
(12) Kormondy, K. J.; Cho, Y.; Posadas, A. B.; Zheng, L.; Lai, K.; Wang, Q.; Kim, M. J.; He, Q.; Borisevich, A. Y.; Downer, M. C.; Demkov, A. A. Piezoelectric Modulation of Nonlinear Optical Response in $BaTiO_3$ Thin Film. *Appl. Phys. Lett.* **2018**, *113*, 132902.
(13) Veithen, M.; Gonze, X.; Ghosez, P. First-Principles Study of the Electro-Optic Effect in Ferroelectric Oxides. *Phys. Rev. Lett.* **2004**, *93*, 187401.
(14) Geusic, J. E.; Levinstein, H. J.; Rubin, J. J.; Singh, S.; Van Uitert, L. G. The Nonlinear Optical Properties of $Ba_2NaNb_5O_{15}$. *Appl. Phys. Lett.* **1967**, *11*, 269.
(15) Levin, I.; Stennett, M. C.; Miles, G. C.; Woodward, D. I.; West, A. R.; Reaney, I. M. Coupling between Octahedral Tilting and Ferroelectric Order in Tetragonal Tungsten Bronze-Structured Dielectrics. *Appl. Phys. Lett.* **2006**, *89*, 122908.
(16) Zhu, X.; Fu, M.; Stennett, M. C.; Vilarinho, P. M.; Levin, I.; Randall, C. A.; Gardner, J.; Morrison, F. D.; Reaney, I. M. A Crystal-Chemical Framework for Relaxor versus Normal Ferroelectric Behavior in Tetragonal Tungsten Bronzes. *Chem. Mater.* **2015**, *27*, 3250−3261.
(17) Abrahams, S. C.; Jamieson, P. B.; Bernstein, J. L. Ferroelectric Tungsten Bronze-Type Crystal Structures. III. Potassium Lithium Niobate $K_{(6-x-y)}Li_{(4+x)}Nb_{(10+y)}O_{30}$. *J. Chem. Phys.* **1971**, *54*, 2355−2364.
(18) Li, K.; Li Zhu, X.; Qiang Liu, X.; Ming Chen, X. Evolution of Structure, Dielectric Properties, and Re-entrant Relaxor Behavior in $Ba_5La_xSm_{1-x}Ti_3Nb_7O_{30}$ (x = 0.1, 0.25, 0.5) Tungsten Bronze Ceramics. *J. Appl. Phys.* **2013**, *114*, No. 044106.
(19) Josse, M.; Heijboer, P.; Albino, M.; Molinari, F.; Porcher, F.; Decourt, R.; Michau, D.; Lebraud, E.; Veber, P.; Velazquez, M.; Maglione, M. Original Crystal-Chemical Behaviors in $(Ba,Sr)_2$Ln-$(Fe,Nb,Ta)_5O_{15}$ Tetragonal Tungsten Bronze: Anion-Driven Properties Evidenced by Cationic Substitutions. *Cryst. Growth Des.* **2014**, *14*, 5428−5435.
(20) Buixaderas, E.; Kempa, M.; Bovtun, V.; Kadlec, C.; Savinov, M.; Borodavka, F.; Vaněk, P.; Steciuk, G.; Palatinus, L.; Dec, J. Multiple Polarization Mechanisms across the Ferroelectric Phase Transition of the Tetragonal Tungsten-Bronze $Sr_{0.35}Ba_{0.69}Nb_2O_{6.04}$. *Phys. Rev. Mater.* **2018**, *2*, 124402.
(21) Feng, W. B.; Zhu, X. L.; Liu, X. Q.; Fu, M. S.; Ma, X.; Jia, S. J.; Chen, X. M. Relaxor Nature in $Ba_5RZr_3Nb_7O_{30}$ (R = La, Nd, Sm) Tetragonal Tungsten Bronze New System. *J. Am. Ceram. Soc.* **2018**, *101*, 1623−1631.
(22) Cerretti, G.; Schrade, M.; Song, X.; Balke, B.; Lu, H.; Weidner, T.; Lieberwirth, I.; Panthöfer, M.; Norby, T.; Tremel, W. Thermal Stability and Enhanced Thermoelectric Properties of the Tetragonal

Tungsten Bronzes $Nb_{8-x}W_{9+x}O_{47}$ (0< x< 5). *J. Mater. Chem. A* **2017**, *5*, 9768−9774.

(23) Allouche, B.; Gagou, Y.; Le Marrec, F.; Fremy, M.-A.; El Marssi, M. Bipolar Resistive Switching and Substrate Effect in $GdK_2Nb_5O_{15}$ Epitaxial Thin Films with Tetragonal Tungsten Bronze Type Structure. *Mater. Des.* **2016**, *112*, 80−87.

(24) Hajlaoui, T.; Harnagea, C.; Michau, D.; Josse, M.; Pignolet, A. Highly Oriented Multiferroic $Ba_2NdFeNb_4O_{15}$-Based Composite Thin Films with Tetragonal Tungsten Bronze Structure on Silicon Substrates. *J. Alloys Compd.* **2017**, *711*, 480−487.

(25) Koo, J.; Jang, J. H.; Bae, B. S. Crystallization Behavior of Sol-Gel-Derived Strontium Barium Niobate Thin Films. *J. Am. Ceram. Soc.* **2001**, *84*, 193−199.

(26) Huang, J.; Gellatly, A.; Kauffmann, A.; Sun, X.; Wang, H. Exchange Bias Effect along Vertical Interfaces in $La_{0.7}Sr_{0.3}MnO_3$:NiO Vertically Aligned Nanocomposite Thin Films Integrated on Silicon Substrates. *Cryst. Growth Des.* **2018**, *18*, 4388−4394.

(27) MacManus-Driscoll, J. L.; Zerrer, P.; Wang, H.; Yang, H.; Yoon, J.; Fouchet, A.; Yu, R.; Blamire, M. G.; Jia, Q. Strain Control and Spontaneous Phase Ordering in Vertical Nanocomposite Heteroepitaxial Thin Films. *Nat. Mater.* **2008**, *7*, 314−320.

(28) Huang, J.; Qi, Z.; Li, L.; Wang, H.; Xue, S.; Zhang, B.; Zhang, X.; Wang, H. Self-Assembled Vertically Aligned Ni Nanopillars in CeO_2 with Anisotropic Magnetic and Transport Properties for Energy Applications. *Nanoscale* **2018**, *10*, 17182−17188.

(29) Huang, J.; Wang, X.; Phuah, X. L.; Lu, P.; Qi, Z.; Wang, H. Plasmonic Cu Nanostructures in ZnO as Hyperbolic Metamaterial Thin Films. *Mater. Today Nano* **2019**, *8*, 100052.

(30) Huang, J.; Li, L.; Lu, P.; Qi, Z.; Sun, X.; Zhang, X.; Wang, H. Self-Assembled Co-$BaZrO_3$ Nanocomposite Thin Films with Ultra-Fine Vertically Aligned Co Nanopillars. *Nanoscale* **2017**, *9*, 7970−7976.

(31) Wang, X.; Jian, J.; Zhou, Z.; Fan, C.; Dai, Y.; Li, L.; Huang, J.; Sun, J.; Donohue, A.; Bermel, P.; Zhang, X.; Chen, H.-T.; Wang, H. Self-Assembled Ag-TiN Hybrid Plasmonic Metamaterial: Tailorable Tilted Nanopillar and Optical Properties. *Adv. Opt. Mater.* **2019**, *7*, 1801180.

(32) Huang, J.; Wang, X.; Hogan, N. L.; Wu, S.; Lu, P.; Fan, Z.; Dai, Y.; Zeng, B.; Starko-Bowes, R.; Jian, J.; Wang, H.; Li, L.; Prasankumar, R. P.; Yarotski, D.; Sheldon, M.; Chen, H.-T.; Jacob, Z.; Zhang, X.; Wang, H. Nanoscale Artificial Plasmonic Lattice in Self-Assembled Vertically Aligned Nitride-Metal Hybrid Metamaterials. *Adv. Sci.* **2018**, *5*, 1800416.

(33) Soergel, E. Piezoresponse Force Microscopy (PFM). *J. Phys. D: Appl. Phys.* **2011**, *44*, 464003.

(34) Zhao, M.-H.; Wang, Z.-L.; Mao, S. X. Piezoelectric Characterization of Individual Zinc Oxide Nanobelt Probed by Piezoresponse Force Microscope. *Nano Lett.* **2004**, *4*, 587−590.

(35) Østreng, E.; Sønsteby, H. H.; Sajavaara, T.; Nilsen, O.; Fjellvåg, H. Atomic Layer Deposition of Ferroelectric $LiNbO_3$. *J. Mater. Chem. C* **2013**, *1*, 4283−4290.

(36) Yuan, Z.; Liu, J.; Weaver, J.; Chen, C. L.; Jiang, J. C.; Lin, B.; Giurgiutiu, V.; Bhalla, A.; Guo, R. Y. Ferroelectric $BaTiO_3$ Thin Films on Ni Metal Tapes Using NiO as Buffer Layer. *Appl. Phys. Lett.* **2007**, *90*, 202901.

(37) Jiang, J. C.; Tian, W.; Pan, X. Q.; Gan, Q.; Eom, C. B. Domain Structure of Epitaxial $SrRuO_3$ Thin Films on Miscut (001) $SrTiO_3$ Substrates. *Appl. Phys. Lett.* **1998**, *72*, 2963−2965.

(38) Qi, Z.; Tang, J.; Huang, J.; Zemlyanov, D.; Pol, V. G.; Wang, H. Li_2MnO_3 Thin Films with Tilted Domain Structure as Cathode for Li-Ion Batteries. *ACS Appl. Energy Mater.* **2019**, *2*, 3461−3468.

https://dx.doi.org/10.1021/acsami.0c03487
ACS Appl. Mater. Interfaces 2020, 12, 23076−23083